

Floquet-Bloch resonances in near-petahertz electroabsorption spectroscopy of SiO₂M. Volkov^{1,*}, S. A. Sato^{2,3}, A. Niedermayr¹, A. Rubio^{3,4}, L. Gallmann¹, and U. Keller¹¹*Department of Physics, ETH Zurich, 8093 Zurich, Switzerland*²*Center for Computational Sciences, University of Tsukuba, Tsukuba 305-8577, Japan*³*Max Planck Institute for the Structure and Dynamics of Matter, Luruper Chaussee 149, 22761 Hamburg, Germany*⁴*Center for Computational Quantum Physics (CCQ), Flatiron Institute, New York 10010, USA*

(Received 14 October 2022; revised 23 December 2022; accepted 23 March 2023; published 5 May 2023)

The electric field of an intense laser pulse can directly modify the electronic properties of materials via electromodulation up to the petahertz regime. In this regime, the energy of the quiver motion of the electron-hole pair is comparable with the photon energy, which results in complex nonadiabatic dynamics. This regime opens opportunities to probe the electronic structure of materials on the attosecond timescale. Here, we show how the quasistatic electromodulation spectroscopy based on the Franz-Keldysh effect (FKE) connects with its nonadiabatic limit, which we find to be determined by resonant transitions between Floquet-Bloch states. This insight can be applied to measure the effective mass, ponderomotive and binding energies of the electron-hole pair on a few-femtosecond timescale. We demonstrate this by experimentally investigating laser-field-driven fused silica, a prototypical material for light-wave electronics, with extreme-ultraviolet attosecond pulse trains. We reproduce the experimental transient absorption spectra with an effective band structure and a dynamical Franz-Keldysh model, offering a simple parametrization for a theoretically challenging but technologically abundant material. *Ab initio* calculations in α -quartz highlight the contributions of specific bands, symmetry, and crystal orientation that are hidden in the experimental data due to randomized crystallographic orientation and finite temporal and spatial coherence. We show that the dynamical FKE can be explained as a third-order nonlinear process in the weak-field regime. The delay-dependent position of the absorption maxima and minima has a minimum tilt angle, determined by transitions between the underlying Floquet-Bloch states. In our analysis, we discuss the main experimental observables and show their connection to the parameters of the solid, providing the basis for nonadiabatic electromodulation spectroscopy.

DOI: [10.1103/PhysRevB.107.184304](https://doi.org/10.1103/PhysRevB.107.184304)**I. INTRODUCTION**

Electromodulation spectroscopy utilizes various electro-optic effects to gain information about the intrinsic properties of solids, such as the effective mass or carrier concentration [1,2]. The direct influence of the electric field on the band structure of semiconductors via the Franz-Keldysh effect (FKE) [3,4] is at the basis of electroabsorption and electroreflectance spectroscopy [2]. In the FKE, the electric field, either external or built-in, transforms the wave function of Bloch electrons into an Airy shape [1]. The tail of the Airy function extends into the band gap region, enabling absorption of photons with energies smaller than the band gap. Above the band gap, the Airy solution results in quasiperiodic oscillations of absorption with the photon energy. By rapidly modulating the electric field and applying lock-in detection, a small

change in absorption can be measured with high precision, allowing a fine characterization of semiconductor electronic structure [2]. The development of the theoretical understanding of the FKE [1,2,5,6] allowed one to determine from the Franz-Keldysh (FK) oscillations the electron effective mass [1], exciton binding energy [7], band structure anisotropy, and valence band splitting [8]. Moreover, analysis of FK oscillations enabled measurements of carrier concentration and the built-in field [9], spatial electron coherence [10] and confinement [11], and observation of coherent phonons [12].

At a high modulation frequency, however, the material response becomes noninstantaneous, allowing us to study nonequilibrium electron dynamics in real time. The high-frequency (dynamical) FKE has been theoretically described in Refs. [13,14] and subsequently observed in the terahertz domain in quantum wells [15,16] and later in semiconductors [17,18]. For these cases, the electric field of an electromagnetic wave was used to modulate the material absorption, opening the possibility of further increasing the modulation frequency into the optical domain. The attosecond dynamical FKE (DFKE) was later observed in polycrystalline diamond [19,20]. It was found that intraband motion dominates the material response, and the observations were in agreement with the DFKE in a parabolic band approximation. Previously, *ab initio* calculations allowed us to reproduce the experiments in dielectrics, semiconductors, and metals [20–23], and SiO₂ was investigated with time-dependent density functional

*mikhail.volkov@mbi-berlin.de

[†]Present address: Max Born Institute for Nonlinear Optics and Short Pulse Spectroscopy, Max-Born-Strasse 2a, 12489 Berlin, Germany.

Published by the American Physical Society under the terms of the [Creative Commons Attribution 4.0 International](https://creativecommons.org/licenses/by/4.0/) license. Further distribution of this work must maintain attribution to the author(s) and the published article's title, journal citation, and DOI.

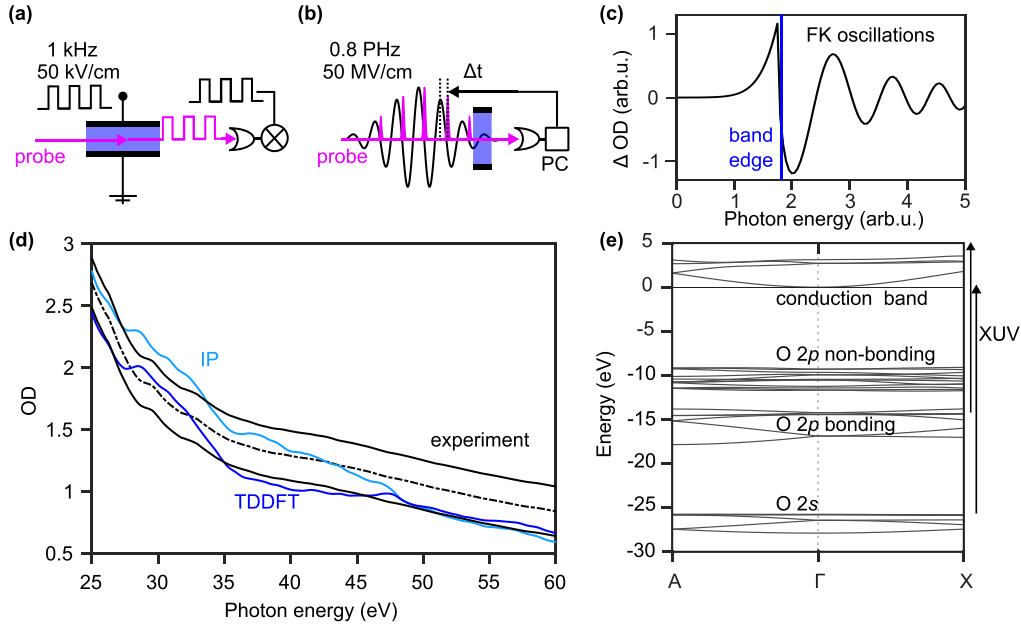


FIG. 1. The principle of petahertz electroabsorption and the electronic structure of SiO_2 . (a) Voltage modulation in electroabsorption spectroscopy. An optical probe (magenta arrow) measures the absorption change in the sample (blue) induced by the electric field bias. The modulated probe is then collected with a homodyne detector. (b) Nonadiabatic electroabsorption, where the sample is modulated at a near-petahertz frequency by the oscillating electric field of light and probed with a delayed and phase-locked attosecond pulse train (APT) with the same periodicity (magenta). (c) Typical differential electroabsorption spectrum, with characteristic Franz-Keldysh (FK) oscillations above the band edge. (d) Optical density of a SiO_2 nanofilm: experimental value (nominal sample thickness 40 nm) compared with time-dependent density functional theory (TDDFT) calculations for a 45-nm film. The independent-particle (IP) model shows qualitative agreement with the full TDDFT calculation. The discrepancy between the two calculations is attributed to the local field effect. (e) Calculated band structure of α -quartz in the Γ -A and Γ -X directions. The dominant contributions from different atomic orbitals are marked according to the literature [38]. The black arrows indicate the possible extreme ultraviolet (XUV) transitions in our probe photon energy range.

theory (TDDFT) in great detail [24–26]. Moreover, recent *ab initio* calculations succeeded in describing attosecond dynamics beyond the FKE [21,22,27,28]. However, a clear connection between the experimental observables and the electronic structure is missing. Here, we provide this connection with a detailed explanation of the so-called *fishbone* shape of the attosecond transient absorption spectra and its relation to the ponderomotive and binding energies of the electron-hole pair. Furthermore, we connect the *fishbone* structure to the spectra measured in conventional quasistatic electroabsorption spectroscopy. With this, we provide a consistent extension of modulation spectroscopy into the nonadiabatic regime, advancing it toward a true analytical technique capable of tracking the electronic structure of solids on a few-femtosecond timescale.

To this end, we apply attosecond transient absorption spectroscopy to study SiO_2 , a pivotal material for telecom and integrated circuits, which is also prototypical in light-wave electronics and petahertz field metrology [29,30]. Previous attosecond transient absorption studies of SiO_2 have focused on absorption dynamics at the Si $L_{2,3}$ edge [31], which is dominated by core-hole exciton effects [32]. Other experimental efforts have utilized high- and low-order harmonic generation, providing insight into the quartz anisotropy and conduction band structure [33–35] and enabled the direct measurement of optical polarization [36]. In contrast, we investigate the valence-to-conduction band transitions in the photon energy

range of 25–50 eV, where the DFKE is expected to provide detailed spectroscopic information about the valence and conduction band structure [20]. We support our experimental investigations with *ab initio* calculations in α -quartz and a parabolic-band model of the DFKE [19]. We find that SiO_2 exhibits a rich spectral response with pronounced non-instantaneous subcycle dynamics. The experimental spectra, however, have fewer features than the *ab initio* calculations due to electron scattering and limited coherence length in the amorphous specimen. The experiment can be reproduced in a DFKE model with an effective band structure. With this model, we find that the attosecond absorption delays within the electric field cycle have an upper quantum limit. In addition, we show that the FK oscillations manifest already in the cycle-averaged absorption spectra as quasiperiodic oscillations with the photon energy and provide a measurement of the reduced electron-hole mass, without the need for subcycle time resolution.

II. EXPERIMENT

A. Petahertz electroabsorption

In low-frequency electroabsorption, a modulation voltage of 10–100 kV/cm allows one to measure small variations from equilibrium absorption in a lock-in acquisition [Fig. 1(a)]. The observed FK oscillations [Fig. 1(c)] are fitted with analytical formulas, with the fit parameters being

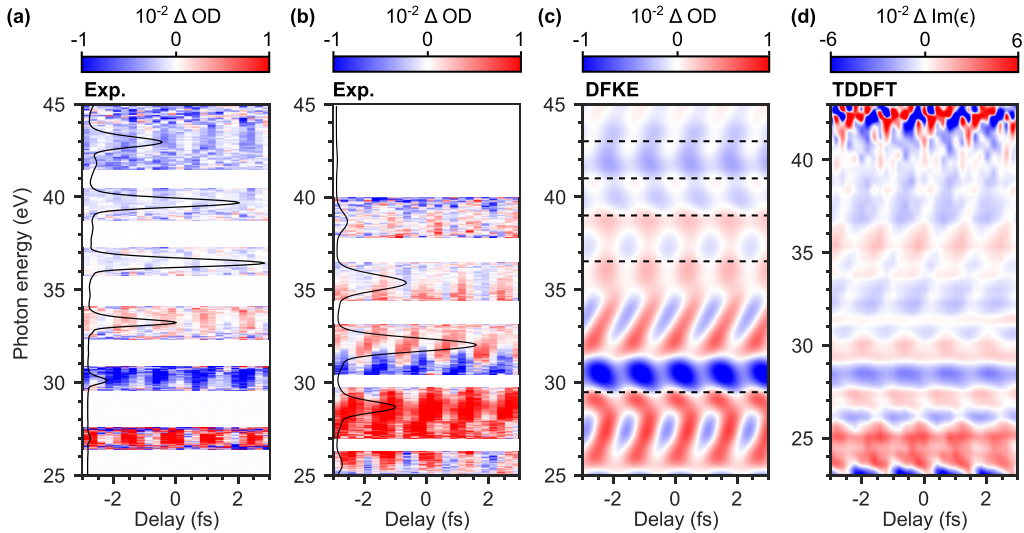


FIG. 2. Experimental transient absorption vs calculation. Transient absorption of polycrystalline SiO_2 with attosecond pulse trains (APTs) generated in (a) argon and (b) xenon. (c) Dynamical Franz-Keldysh effect (DFKE) calculation, with the band parameters specified in Table I. Dashed lines indicate the modeled band edges. (d) *Ab initio* calculation of the orientation-averaged response of α -quartz. Note that the energy axis in (d) is shifted by 2 eV with respect to the other panels.

the band edge, reduced mass, and the electric field strength. For example, higher field strength or lower reduced electron-hole mass result in lower periodicity of the FK oscillations [2]. Petahertz electroabsorption [Fig. 1(b)] uses electric fields three orders of magnitude higher than its low-frequency counterpart and a probe pulse of subcycle duration or a train of attosecond pulses phase-locked to the pump electric field. Such a field strength surpasses the dielectric breakdown of the material. However, the high modulation frequency (0.8 PHz) allows one to apply a field strength of $\sim 1 \text{ V/\AA}$ briefly without damaging the material, thereby opening a strong-field regime of light-matter interaction to spectroscopic investigation. This approach allows one to measure the electron-hole structure on a few-femtosecond timescale in a wide energy range, including unoccupied states high in the conduction band, and thereby to track the electronic structure dynamics during ultrafast phase transitions.

B. Equilibrium absorption spectrum

The transient absorption experiments were carried out on the attosecond beamline described extensively in previous works [20,37]. The near-infrared (NIR) pump pulse with a center photon energy $\hbar\Omega$ of 1.55 eV is in the few-cycle regime with a stabilized carrier-envelope offset phase. The pulse is focused onto a freestanding SiO_2 nanofilm (SiMPore, TEMwindows, nominal thickness 40 nm), with a maximum pulse energy of $10 \mu\text{J}$ and corresponding peak intensity of $7 \pm 2 \text{ TW/cm}^2$. We probe the sample response via changes in the transmission spectrum of attosecond pulse trains (APTs) with a photon energy $\hbar\omega$ of 25–50 eV that are generated in xenon or argon.

The equilibrium optical density (OD) of a SiO_2 film [Fig. 1(d)] shows a reasonable agreement with the first-principles calculations based on TDDFT (see Appendix B) if the nominal thickness of 40 nm is adjusted to 45 nm in the calculations. The discrepancy is not unexpected since the

nominal film thickness is not measured directly but estimated from mass measurements during deposition. High absorption of SiO_2 in the extreme ultraviolet (XUV) range requires high XUV photon flux and the use of large-area ($>50 \mu\text{m}$) nanofilms that are difficult to obtain in a crystalline form.

In the TDDFT calculation, we compare the full model [Fig. 1(d), blue] with an independent particle (IP) prediction [Fig. 1(d), light blue]. A small deviation in the lower-energy part of the spectrum is expected to be due to local field effects. Figure 1(e) shows the calculated band structure of α -quartz, where XUV photons (black arrows) can induce transitions from the oxygen $2s$ states to the bottom of the conduction band, as well as transitions from the oxygen $2p$ states high into the conduction band. Extensive literature established that the primary difference between different allotropic modifications of SiO_2 is the angle of the Si-O-Si bond [39]. Moreover, the band structure of crystalline and amorphous SiO_2 is similar [39] because it is not sensitive to the long-range order [38]. The highest valence band is composed of oxygen lone-pair (nonbonding) orbitals, dominated by oxygen p states, oriented along the Si-O-Si axis. The middle of the valence band is composed of bonding Si-O orbitals, separated by the ionic gap from the lowest band that is composed mostly of O $2s$ -orbitals.

C. Nonequilibrium absorption spectra

Figures 2(a) and 2(b) show experimental transient absorption spectra obtained at a pump intensity of 7 TW/cm^2 . The color plot shows changes in material OD, calculated as a logarithm of the ratio of the transmitted spectra with and without the pump, yielding a differential signal, as in conventional electroabsorption spectroscopy. The signal is robust with respect to the specific shape and duration of probe APTs. To obtain a complete spectral coverage at identical pumping conditions, we use XUV pulses generated in argon [Fig. 2(a)] and xenon [Fig. 2(b)]. Overlaid black lines show the transmitted probe spectra; noisy areas with low XUV

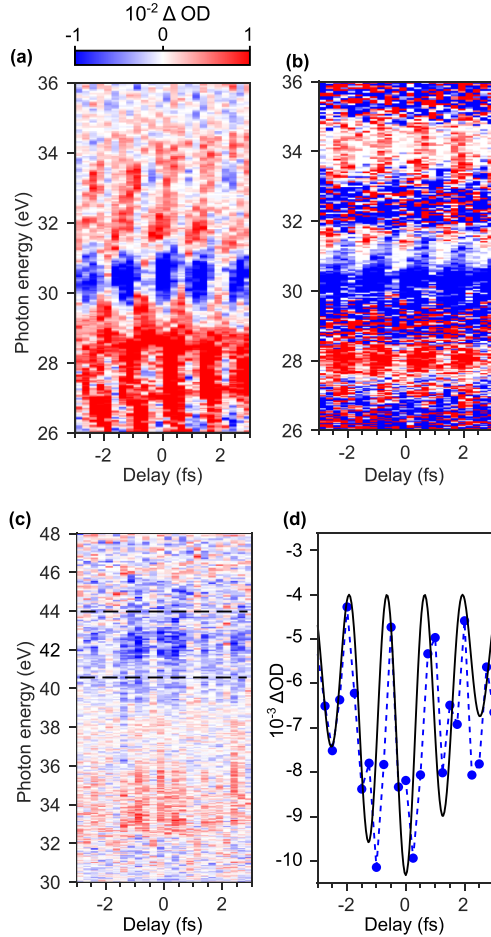


FIG. 3. Additional transient absorption data. (a) Measurement taken with continuous extreme ultraviolet (XUV) pulse spectrum generated in xenon. (b) Measurement in a different 100-nm sample from a different supplier. (c) Measurement taken with single attosecond pulse (SAP), note the different energy axis. (d) SAP signal integrated between 40.5 and 44 eV [dashed lines in (c)].

counts are blanked out. Together, Figs. 2(a) and 2(b) provide a complementary spectral mapping of a wide photon energy region. The data furthermore agree with additional measurements taken in a 100-nm-thick sample from a different supplier [Fig. 3(b)] and a measurement with a continuous XUV spectrum [Fig. 3(a)]. Using APTs generated under different conditions helps to complete the spectral mapping. We characterize the attosecond pulses via reconstruction of attosecond beating by interference of two-photon transition [40] measurement in neon and find that the APT consists of six 270-as bursts on average. The strongest transient signal is observed at 25–35 eV, where the XUV absorption is very high, impeding a reliable measurement with single attosecond pulses with our experimental parameters [Fig. 3(c)]. Thus, our choice of APTs as a probe provides a broader spectral coverage but does not provide the absolute delays with respect to the pump electric field. This is in contrast to the previous measurements in diamond and GaAs [20,21] for which we used a single attosecond pulse with which we could measure the time-dependent electric field with attosecond streaking

TABLE I. Effective band parameters for the empirical DFKE model. μ_{eh} is the reduced effective electron-hole mass in units of the free electron mass m_e , given by $\mu_{eh}^{-1} = m_e^{*-1} + m_h^{*-1}$, and m_e^* and m_h^* are the effective masses of the electron and hole.

Energy (eV)	μ_{eh} (m_e)
23	0.41
29.5	0.56
36.5	0.22
39	0.22
41	0.22
43	0.22

[20,21]. However, as we will show in the discussion that knowledge of the absolute delays is not required to characterize the electronic structure of the material. The APTs are locked to the electric field oscillations; however, every train probes a different part of pump pulse envelope, resulting in an effective average over a range of E -field amplitudes.

The transient absorption exhibits a 2Ω modulation directly corresponding to the 0.8 PHz frequency of the electric field of the pump laser. The transient absorption exhibits a pronounced dispersion, i.e., delay-dependent position of the absorption maxima and minima which show up with tilted red or blue features. These features are indicative of a noninstantaneous response that does not depend on the probe spectra and is therefore an intrinsic characteristic of the material.

D. Dynamical FK model

Figure 2(c) shows simulated transient absorption with a peak field strength of 0.9 V/Å, based on the DFKE model [19,20] with additional 1-eV broadening to account for finite lifetime. Our calculations accurately reproduce the results of the original model [19] as well as subsequent two-band calculations in diamond [20,41]. Here, the main features of the SiO₂ spectra, namely, the amplitude, energy position, width, and tilt of the 2Ω periodic oscillations are reproduced assuming an effective band structure consisting of six band pairs (Table I). The photon energy range corresponds to transitions from oxygen 2s and 2p levels to the conduction band, with electron effective mass ranging between 0.5 and 1 m_e and hole effective mass between 0.4 and 7 m_e according to the literature [38], which correspond to a reduced electron-hole mass μ_{eh} in the range of 0.22–0.87 m_e . The DFKE model therefore allows us to model an octave-spanning response of SiO₂ in the XUV with simple parametrization. We note, however, that since the DFKE spectral shape is derived from Airy functions that form a complete basis set, including more bands can yield even better quantitative agreement with the experiment, at the expense of model simplicity.

E. *Ab initio* calculations

Figure 2(d) shows the results of *ab initio* simulations of the pump-probe experiment in α -quartz, see Appendix B. To emulate fused silica, we perform orientation averaging that restores the inversion symmetry that is broken in α -quartz. The broken symmetry manifests as Ω -periodic oscillations of the absorption along the crystal c axis (Fig. 4). We identify

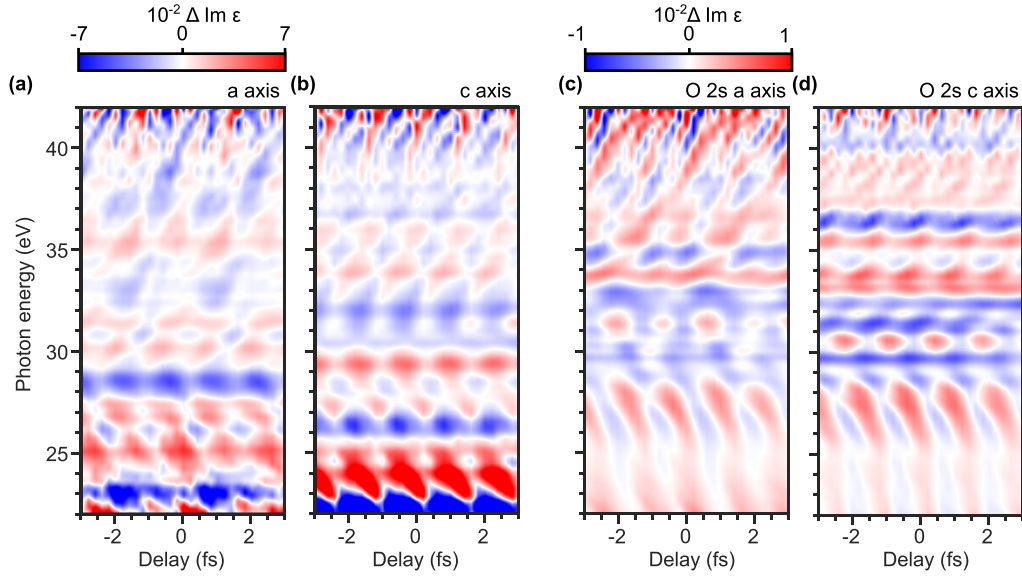


FIG. 4. *Ab initio* calculations of transient absorption in α -quartz. Electric field along the (a) a axis and (b) c axis. (a) shows Ω -periodic oscillation due to broken inversion symmetry. Transitions only from the O 2s level for the (c) a axis and (d) c axis.

similar absorption and transparency regions [red and blue, Fig. 2(d)] as in the experiment if the calculated spectrum is shifted down by 2 eV. Since accurate determination of the energy position is problematic in TDDFT with approximated functionals, the required energy shift is not unexpected. However, the experimental data are overall simpler, exhibiting fewer spectral features. We attribute the less detailed features to scattering and limited coherence length in the polycrystalline sample. Similarly, in electromodulation, the crystalline quality of the samples determines the number of the observed FK oscillations [10], and scattering results in plain spectra.

To understand the influence of individual valence bands, we further perform decomposition of the theoretical spectra [42], isolating the contribution of the semicore O 2s level.

We find that, although O 2s levels contribute significantly, the O 2p-CB transitions cannot be discarded from the analysis (Fig. 4). To connect the TDDFT results and the empirical model, we extract the electron and hole effective masses from the theoretical band structure in the Γ -A direction, corresponding to the c axis of α -quartz. Here, 60 band pairs contribute to the signal in the experimentally accessible range of 25–45 eV. We calculate the DFKE parabolic-band model for a simplified band structure, obtained by k-means clustering (Appendix C). We find that a noninteracting parabolic band DFKE model reproduces most TDDFT features (Fig. 5), in agreement with the hypothesis of dominant intraband contribution [20]. However, in contrast to the results reported in diamond [20], we find that it is not possible to define a

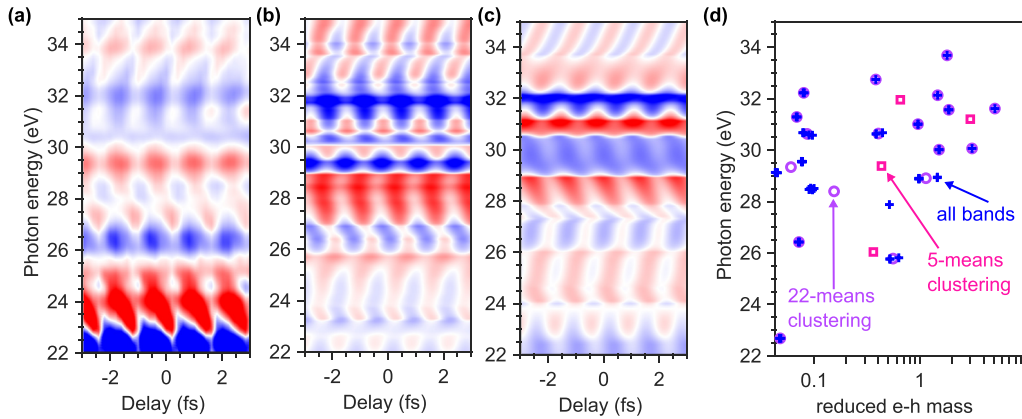


FIG. 5. Parabolic band approximation and simplified band structure. (a) Time-dependent density functional theory (TDDFT) calculation along the quartz c axis (Γ -A direction). (b) Dynamical Franz-Keldysh effect (DFKE) in parabolic approximation with the TDDFT bands fitted to obtain band effective mass and band edges. 60 band pairs [(d), blue crosses] are reduced to 22 pairs [(d), violet circles] via k-means clustering. (c) DFKE in parabolic approximation with 5 bands only [(d), magenta squares]. (d) The band pairs from TDDFT, obtained via parabolic fits (blue crosses) and the k-means clustering results for 22 bands (violet circles), and 5 bands (magenta squares). The bands pairs <22 eV not shown, but their impact on transient absorption >22 eV is included.

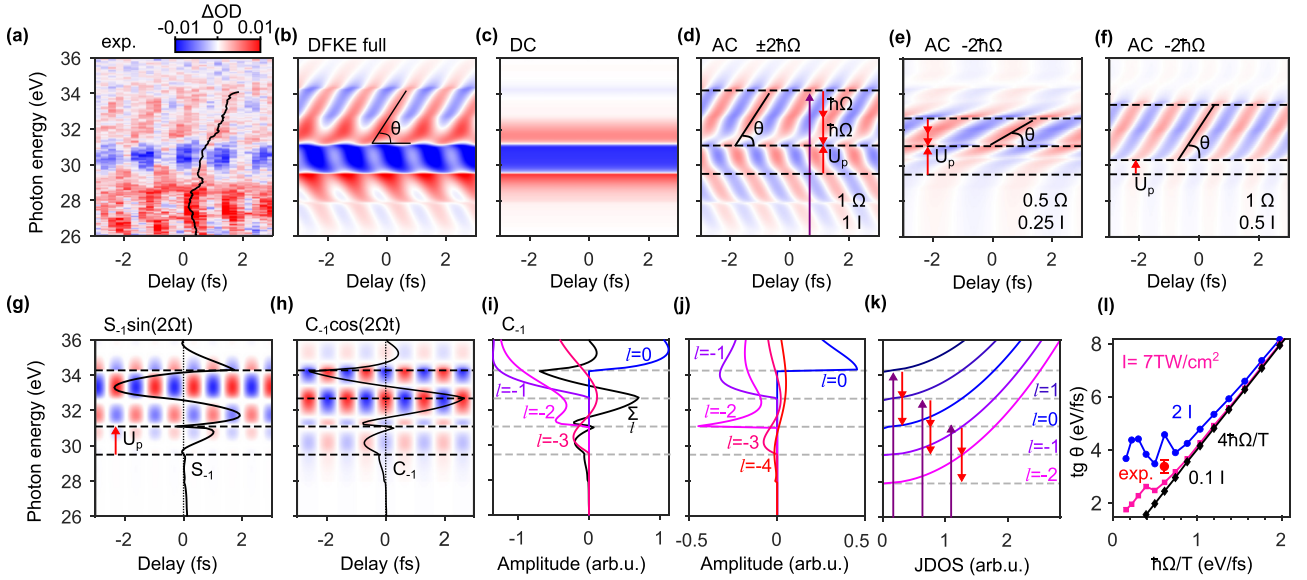


FIG. 6. Dynamical Franz-Keldysh effect (DFKE) decomposition and its quantum limit. (a) Experimental transient absorption spectra. Black curve shows the oscillation phase obtained by Fourier filtering the spectrogram at the frequency of 2Ω . (b) DFKE calculated with $E = 0.9 \text{ V/\AA}$, $\mu_{eh} = 0.4 m_e$, $E_{BG} = 29.5 \text{ eV}$. (c) DC and (d) AC parts of the DFKE signal. Arrows indicate the extreme ultraviolet (XUV; violet) and pump (red) transitions. (e) $-2\hbar\Omega$ component of the AC part, calculated at half the pump frequency and quarter intensity, thus matching the U_p value in (d) and the apex position of the *fishbone* structure. (f) Same signal as in (e) at half the pump intensity. (g) Sine component of the upper AC branch signal, oscillating in phase with the pump electric field. Black curve shows the amplitude of the S_{-1} coefficient in arbitrary units. Black dashed lines indicate the band gap (29.5 eV), the *fishbone* apex (31.09 eV), and its upper edge (34.27 eV). (h) Corresponding cosine (out-of-phase) component of the upper AC branch and its amplitude C_{-1} (black curve). (i) Floquet-Bloch decomposition of the C_{-1} amplitude (black). Colored curves show the contributions of Floquet states with an index l . (j) Amplitudes of three-photon transitions, shown in (d) and (k) as arrows, with the final Floquet-Bloch state l of the electron-hole pair. (k) Joint density of states of the Floquet-Bloch states l . (l) Tilt angle of the *fishbone* structure plotted against photon energy per optical cycle [see Eq. (3)]. The line at 0.7 TW/cm^2 coincides with the theoretical limit given by $4\hbar\Omega/T$. Red point shows the experimental tilt value from the upper *fishbone* branch in (a).

single dominant transition. Therefore, we conclude that the empirical parameters found in the DFKE model represent an effective response of fused silica, including randomized orientation and scattering. The extracted parameters thus do not necessarily correspond to specific electronic bands. Such an effect is intrinsic to photoabsorption measurements, where a selected photon energy may involve several electronic transitions, while in photoelectron spectroscopy, on the other hand, different photons can produce electrons with the same final energy.

III. DISCUSSION

The dynamical FKE has previously been observed at optical frequencies in diamond [20], revealing the characteristic time-energy dependence of the transient spectra, dubbed the *fishbone* structure [43]. Similar dispersion of the modulations was also observed in an exciton system [28], in quantum wells under terahertz radiation [44], and in several theoretical works on attosecond transient absorption of solids [43,45–47]. We find that the response of SiO_2 is more complex than in diamond since we employ ~ 3 times higher pump intensity, while the reduced e - h mass is ~ 3 times lower, resulting in a much higher ponderomotive potential and nonperturbative behavior with $\gamma = U_p/\hbar\Omega \sim 1$. To gain a better understanding of the spectral features, we focus on the photon energy range between 26 and 36 eV, which we probe with a dedicated continuous XUV spectrum (Appendix A), where our empirical

DFKE model within the effective band structure derived in the previous section has only one band edge at 29.5 eV with a reduced mass of $0.4 m_e$.

We find good agreement between the experiment [Fig. 6(a)] and a simplified, two-band DFKE calculation [Fig. 6(b)] exhibiting the *fishbone* structure [20]. To gain better insight into the origin of these spectra, we revisit the DFKE model [19], where the transient absorption signal is given by the real part of conductivity σ :

$$\text{Re}\sigma_{2m}(\omega, t) = \frac{a}{\omega + 2m\Omega} [C_{2m\Omega} \cos(2m\Omega t) + S_{2m\Omega} \sin(2m\Omega t)]. \quad (1)$$

Here, a is a frequency-independent factor, Ω and ω are pump and probe frequencies, $2m$ is the number of an even harmonic of the pump, with $|m| = 0, 1, 2, \dots$. In the present experiment, as well as in the previous studies [20,21], only the 2Ω component of transient absorption is observed; therefore, we neglect terms $|m| > 1$ in the following analysis. Spectral amplitudes $C_{0;\pm 2\Omega}$ and $S_{0;\pm 2\Omega}$ are calculated as orientation-averaged transition amplitudes that contain resonant terms in the form:

$$\hbar\omega = E_{\text{gap}} + \frac{k^2}{2\mu_{eh}} + U_p + l\hbar\Omega + 2m\hbar\Omega. \quad (2)$$

Here, E_{gap} is the band gap, k is the quasimomentum, and U_p is the ponderomotive energy. The equation represents energy conservation in a three-photon transition (one XUV $\hbar\omega$ and two pump photons $2\hbar\Omega$) between Floquet-Bloch states

$(E_{\text{gap}} + \frac{k^2}{2\mu_{eh}} + l\hbar\Omega)$ with an index l . The U_p term is due to the extra quiver energy of the electron-hole pair that is not present in the bound state, see, e.g., Ref. [48]. The real part of the conductivity, corresponding to absorption, can therefore be presented as a summation of time-independent DC [$m=0$, Fig. 6(c)] and time-dependent AC components [$m=\pm 1$, Fig. 6(d)]. The AC component is composed of two terms representing emission of two pump photons [$m=-1$, upper branch of the *fishbone*, photon energy >31 eV in Fig. 6(d)] and absorption of two pump photons ($m=1$, lower branch, photon energy <31 eV).

The apex of the *fishbone* structure emerges at U_p above the band gap, and the signal with a 2Ω periodicity stretches to $2\hbar\Omega$ above (below) it [Fig. 6(d), black dashed lines]. In Fig. 6(e), we repeat the calculation at half the pump photon energy, and quarter intensity, to match the ponderomotive potential in panel (d). We see that lower pump frequency results in a lower tilt angle θ , in agreement with previous findings in diamond [20]. Specifically, we find that reducing the pump frequency by half results in a 4 times smaller tilt. At the same time, the apex of the *fishbone* coincides in both panels (d) and (e), confirming that the apex position is defined by the ponderomotive upshift from the band edge. In contrast, calculation at the same frequency as in panel (d) but with half the intensity results in a downshift of the *fishbone* apex by a half with respect to the band edge.

To understand the origin of the *fishbone* branches, we decompose the absorption signal into its sine and cosine components according to Eq. (1). Figures 6(g) and 6(h) show the corresponding components oscillating in phase [sine, Fig. 6(g)] and out of phase [cos, Fig. 6(h)] with the pump electric field. We see that, in addition to the time-periodicity of 2Ω , the signal is also $2\hbar\Omega$ periodic in photon energy. Moreover, the amplitudes of the sine and cosine components S_{-1} and C_{-1} (here, the index -1 means emission of two pump photons) oscillate out of phase in photon energy, as evident in Fig. 6(g) in the red and blue color spacing at a fixed delay and the amplitudes S_{-1} and C_{-1} plotted as black curves atop. We note that, from the derivation of the S_m and C_m coefficients [19], it follows that they are Hilbert transform pairs and, for a fixed time delay, correspond to real and imaginary parts of the complex conductivity, which are connected via Kramers-Kronig relations. The combination of time- and photon-energy-periodic signals that oscillate out of phase therefore results in the tilted *fishbone* structure, with a tilt angle given by

$$\tan(\theta)_q = \frac{2\hbar\Omega}{0.5T} = \frac{2}{\pi} \hbar\Omega^2. \quad (3)$$

The 2Ω time periodicity is trivially explained as a direct driving of the system with the electric field cycles in an inversion-symmetric system, as implicitly assumed by orientation-averaged transition amplitudes in the DFKE model [19]. To understand the photon-energy periodicity, we further decompose the C_{-1} component into contributions from specific Floquet-Bloch states with the Floquet numbers l . Figure 6(i) shows the C_{-1} amplitude as a black curve, resulting from summation over all Floquet numbers. From Fig. 6(i), we see that only a few Floquet states with indices $l=-3$ to $l=0$ contribute to the C_{-1} amplitude, depicted

as blue, violet, and magenta curves. The contributions from individual Floquet-Bloch states are a product of their joint density of states (JDOS) and the transition amplitudes: $C_{-1} = \sum_l A_{l,-1} \text{JDOS}_{l,-1}$ in the aforementioned three-photon process, involving absorption of one XUV photon and emission (for the upper *fishbone* branch) or absorption (for the lower *fishbone* branch) of two pump photons, see the violet and red arrows in Fig. 6(k). In this process, l is the index of the final Floquet-Bloch state. For example, the absorption signal at 32.5 eV, that is $\hbar\Omega + U_p$ above the band gap, results from transition to the Floquet-Bloch state with $l=-1$. We therefore conclude that the $2\hbar\Omega$ periodicity of the Fourier amplitudes in photon energy, and thereby the *fishbone* tilt, originate from the $\hbar\Omega$ spacing of the underlying Floquet states.

To quantify the dependence of the tilt angle θ on the pump parameters, we calculate the spectral phase of the upper ($-2\hbar\Omega$) branch for a range of pump frequencies and intensities and compare it with the experimental data. Figure 6(l) shows the extracted tilt angles for pump intensities of $I = 0.7, 7$, and 14 TW/cm², as a function of photon energy per oscillation period. We find that the tilt angle θ is primarily determined by the pump frequency. The extracted tilts at the pump intensity of $I = 0.7$ TW/cm² (or lower) exactly coincide with Eq. (3) for all calculated photon energies. However, increasing the pump intensity for a given pump frequency results in larger angles. To explain this tendency, we note that high intensities result in larger values of the nonperturbative intensity parameter $\gamma = U_p/\hbar\Omega$ [49], corresponding to a more classical (adiabatic) regime. We can approximate the tilt angle in the classical limit as the maximum kinetic energy gain of the electron-hole pair that happens over a quarter of the field cycle since the kinetic energy peaks at twice the driving frequency:

$$\tan(\theta)_c = \frac{4U_p}{\pi} \Omega. \quad (4)$$

These quantum and classical expressions are connected via the nonperturbative intensity parameter γ [49], which is on the order of 1 in our experiments:

$$\frac{\tan(\theta)_c}{\tan(\theta)_q} = 2\gamma. \quad (5)$$

Here, $\tan(\theta)_{c,q}$ have the effective units of power, with the values of 4.9 and 2.44 eV/fs, respectively. Increasing the ponderomotive potential, either with intensity or by lowering the pump frequency, results in larger tilt angles [Fig. 6(l), blue and magenta curves]. To further confirm our understanding of the minimum tilt angle, we compute higher-order components of the signal oscillating at 4Ω that are not observed in the experiment due to their low amplitude relatively to the dominant 2Ω signal, see Appendix D. We find that 4Ω oscillations also exhibit a *fishbone* structure [Figs. 7(e) and 7(g)], with a tilt given by $4\hbar\Omega^2/\pi$ that is twice as high as for the 2Ω oscillation but not four times as high since the photon-energy periodicity given by the Floquet-Bloch spacing is not changed.

The experimental tilt angle is obtained from the spectrogram in Fig. 6(a) by calculating the spectral phase at the 2Ω frequency [Fig. 6(a), black curve] in the photon energy range between 31 and 34 eV, where the influence of lower bands is minimal. We find that the experimental value [Fig. 6(h), red

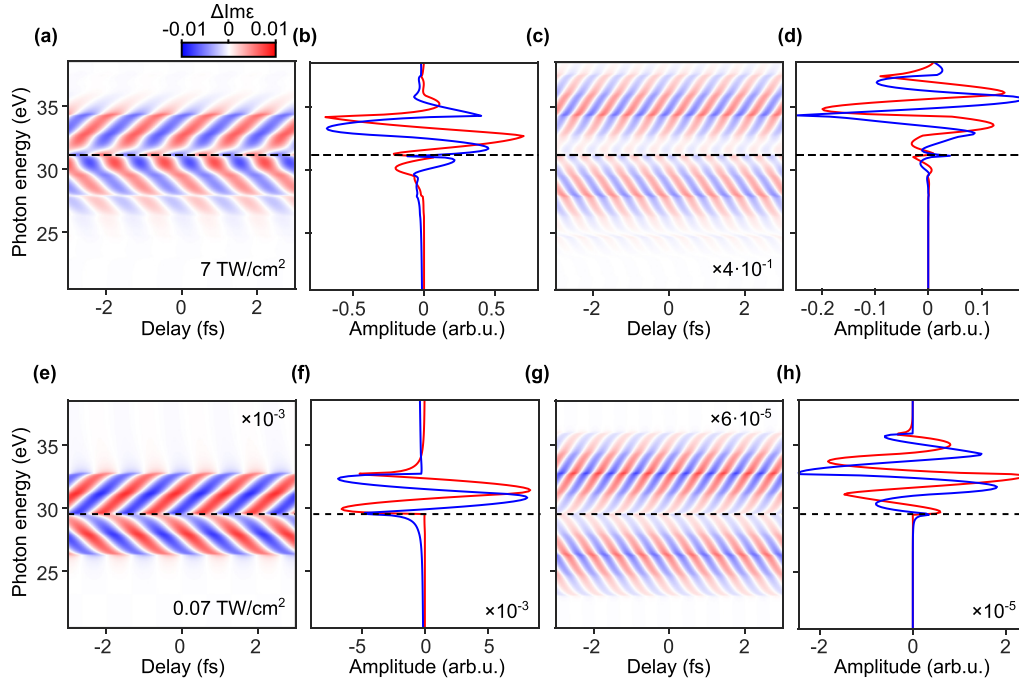


FIG. 7. AC part of the dynamical Franz-Keldysh effect (DFKE) signal calculated for 7 TW/cm² (upper row) and 0.07 TW/cm² (lower row). (a) 2Ω component, dashed line is drawn at U_p (1.59 eV) above the band edge (29.5 eV). (b) Sine (blue) and cosine (red) spectral amplitudes of the 2Ω component. (c) and (d) Same for the 4Ω component. (e)–(h) Same as (a)–(d), at $\times 100$ lower pump intensity. The sine and cosine amplitudes oscillate out of phase in photon energy. The periodicity of these oscillations is equal to $2\hbar\Omega$ in all cases.

circle] is in a good agreement with the presented theory, given the uncertainty of pump intensity measurement in the sample. Therefore, the attosecond delays observed in the transient absorption measurements are primarily determined by the ponderomotive potential that offsets the *fishbone* shape from the band edge and the tilt angle. Under perturbative conditions ($\gamma < 1$), the DFKE spectra are expected to have a universal shape, with the tilt determined by the pump frequency alone. In the nonperturbative (adiabatic) regime ($\gamma > 1$), the tilt can be additionally increased, reducing the observed delays toward more instantaneous response.

In summary, our analysis of the DFKE model shows that transient absorption data exhibit three main observables, with a clear physical interpretation, namely: (i) the apex of the *fishbone* spectral shape, (ii) the *fishbone* tilt, and (iii) the time-integrated absorption profile. These observables are robust against variation of the probe spectra, APT burst duration, or the absolute value of the pump-probe delay. We have shown that the apex position with respect to the band edge is equal to the ponderomotive energy of the electron-hole pair. The deviation of the tilt angle from its perturbative lower limit is a measure of the adiabaticity of the interaction.

IV. PERTURBATIVE APPROXIMATION TO THE DFKE

We have shown that the *fishbone* shape of the DFKE as a function of delay and energy converged in the perturbative limit $\gamma < 1$ to a basic shape with 2Ω delay and $2\hbar\Omega$ energy periodicity and a total energy width of $4\hbar\Omega$. In this section, we explain this shape in terms of a third-order nonlinear process.

We derive algebraic expressions for the DFKE in terms of third-order susceptibility $\chi^{(3)}$ in the low-field regime (see Appendix E). Transient absorption calculated with the derived $\chi^{(3)}$ reproduces the *fishbone* shape, with an approximation error of $< 4\%$ for $\gamma = 0.01$ (Fig. 8). The effective change of linear susceptibility is

$$\Delta\chi^{(1)}(\omega, T) = \chi^{(3)}(\omega, \Omega, -\Omega)E_0^2 + \chi^{(3)}(\omega, \Omega, \Omega)E_0^2e^{i2\Omega T} + \chi^{(3)}(\omega, -\Omega, -\Omega)E_0^2e^{-i2\Omega T}, \quad (6)$$

where Ω and ω are pump and probe frequencies, T is the pump-probe delay, and E_0 is the pump electric field amplitude. The first term in Eq. (6) corresponds to the pump-induced Kerr contribution to linear probe absorption [50] that has been observed in conventional transient absorption spectroscopy [51]. However, the rapidly oscillating terms are usually ignored [52], and their detection requires subcycle time resolution. The transient absorption signal is proportional to the imaginary part of the susceptibility:

$$\begin{aligned} \text{Im}\Delta\chi^{(1)}(\omega, T) &= E_0^2 \text{Im}\chi^{(3)}(\omega, \Omega, -\Omega) \\ &+ E_0^2 \text{Im}[\chi^{(3)}(\omega, \Omega, \Omega) + \chi^{(3)}(\omega, -\Omega, -\Omega)] \cos(2\Omega T) \\ &+ E_0^2 \text{Re}[\chi^{(3)}(\omega, \Omega, \Omega) - \chi^{(3)}(\omega, -\Omega, -\Omega)] \sin(2\Omega T). \end{aligned} \quad (7)$$

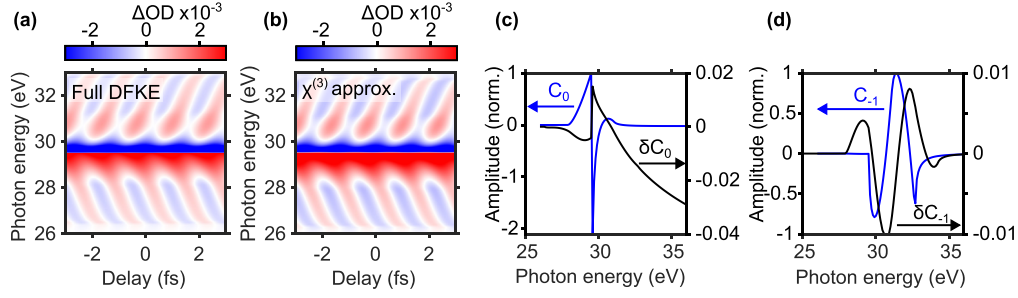


FIG. 8. Perturbative approximation to the dynamical Franz-Keldysh effect (DFKE) as a $\chi^{(3)}$ process. (a) Full DFKE calculation, $\gamma = 0.01$. (b) Perturbative approximation via Eqs. (E18)–(E21). (c) The DC component from the full DFKE calculation (blue line) and the difference from $\chi^{(3)}$ approximation (black line). (d) Same as (c), for the AC ($-2\hbar\Omega$) component.

We thus retrieve the functional form of Eq. (1) and Figs. 6(g) and 6(h) and conclude that the *fishbone* shape originates from mixing of the real and imaginary terms of the third-order susceptibility. Due to Kramers-Kronig relations, peaks of $\text{Im}\chi^{(3)}$ coincide with zeros in $\text{Re}\chi^{(3)}$ and vice versa, thus giving rise to the checkerboard pattern in Figs. 6(g) and 6(h). We note that the electronic response to the pump field alone is instantaneous since its photon energy is far from resonance. In contrast, the electronic response to the XUV field is noninstantaneous at the interband resonance. The mixed electronic response to XUV and NIR fields inherits the noninstantaneous nature of resonant XUV absorption. We therefore conclude that the pump field realizes coherent control of linear XUV absorption via additional three-photon interactions mediated by interband resonances at ω , $\omega \pm \Omega$, $\omega \pm 2\Omega$. These resonances can be seen in the Floquet-Bloch energy levels [Figs. 6(i)–6(k)] and are also explicit in the functional form of $\chi^{(3)}$, see Appendix E.

V. NONADIABATIC QUENCHING OF FK OSCILLATIONS

In this section, we show how the main electromodulation observable, namely, the FK oscillations, manifests in the dynamical regime. Here, we also focus on the electronic band located at 29.5 eV. Figure 9(a) shows how the DFKE spectra change from the nonadiabatic regime at $\Omega = 3.1$ eV [Fig. 9(a), $\gamma = 0.13$] to the adiabatic regime at $\Omega = 0.75$ eV [Fig. 9(b), $\gamma = 8$]. We find that the latter can be closely

approximated by a fully adiabatic calculation based on the standard FK model used in electroabsorption spectroscopy [2], assuming an instantaneous reaction to the sinusoidal electric field [Fig. 9(c)]. While the cycle-averaged DFKE profile coincides with the adiabatic profile at $\gamma = 0.13$ (Fig. 9(d), magenta and black-dashed curves), we observe a strong deviation from adiabatic regime at $\gamma = 8$ (Fig. 9(d), blue curve).

Specifically, the nonadiabatic calculation (Fig. 9(d), blue curve) shows only one FK oscillation with a strongly squeezed period. We argue that such squeezing of the FK oscillations at high pump frequency reflects smaller ponderomotive energy. In the adiabatic limit, the number of FK oscillations is determined by the maximum energy that the electron-hole pair gains before scattering. Counting the number of FK oscillations n allows one to measure the spatial coherence length via the simple relation $l_{\text{coh}} = n\Lambda_{\text{FK}}/eF$, where Λ_{FK} is the oscillation period, F is the electric field strength, and e is the electron charge [10]. The FK oscillation period Λ_{FK} can be derived using asymptotic approximations of the Airy function nodes [1], and for the first oscillation, it is given by

$$\Lambda_{\text{FK}} = \left[\frac{(3\pi eF\hbar/8)^2}{2\mu_{eh}} \right]^{1/3}. \quad (8)$$

This relation is perfectly fulfilled in high-crystallinity samples under a homogenous low-frequency field [33]. In the dynamical regime, maximum gained energy is additionally

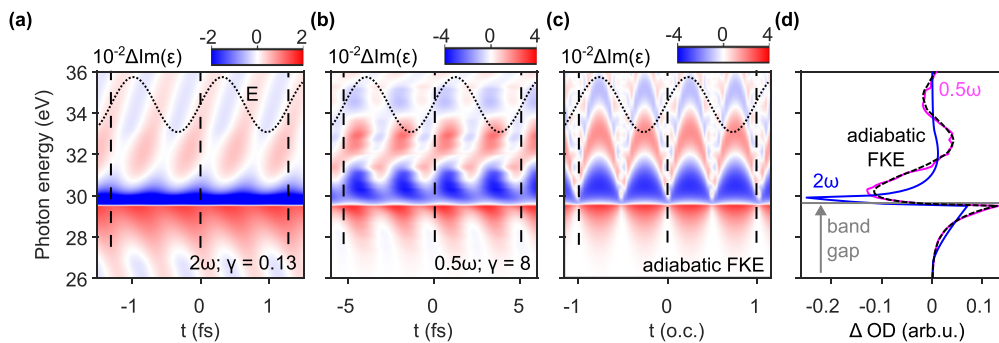


FIG. 9. Nonadiabatic and adiabatic calculations of the dynamical Franz-Keldysh effect (DFKE). (a) DFKE calculation in the nonadiabatic regime, $\Omega = 3.1$ eV, $\gamma = 0.13$. The dotted line shows the phase of the assumed electric field. (b) Adiabatic regime of DFKE, $\Omega = 0.75$ eV, $\gamma = 8$. (c) Fully adiabatic calculation with the standard electroabsorption equations, assuming instantaneous response to the E -field. (d) Cycle-averaged spectral profiles of the corresponding calculations.

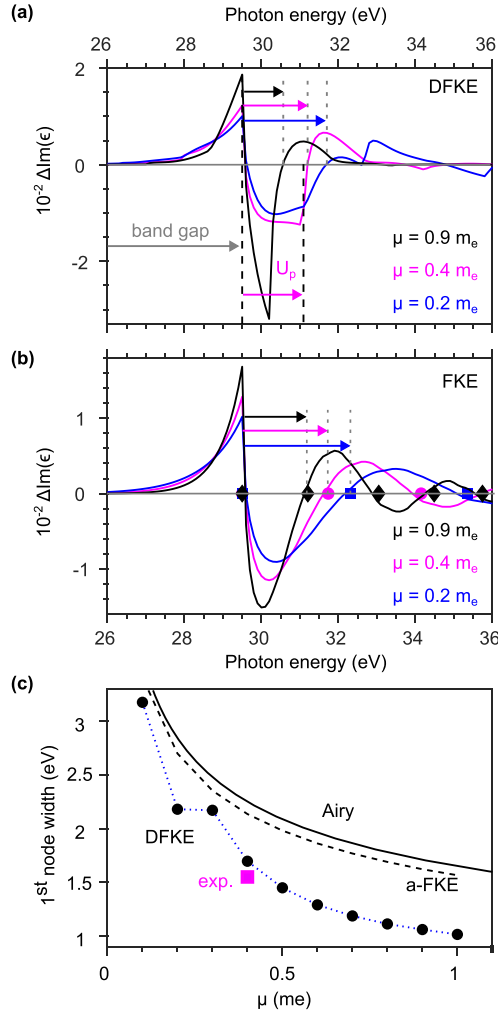


FIG. 10. Franz-Keldysh (FK) oscillations in the cycle-averaged spectra. (a) Cycle-averaged dynamical FK effect (DFKE) spectra computed for the reduced e - h mass of 0.9, 0.4, and 0.2 m_e . The band gap is 29.5 eV, the pump photon energy is 1.55 eV, and the field strength is 0.9 V/Å. Dashed lines show the oscillation period. (b) Same calculation with the fully adiabatic FK equations. Black diamonds, magenta circles, and blue squares show the prediction calculated with eq. (11) of Ref. [1]. (c) Dependence of the first node width (half oscillation period) on the reduced mass. The magenta square shows the experimental value. The continuous line is given by Eq. (8), and the dashed line shows the results of a cycle-averaged fully adiabatic calculation.

limited by the quiver period that amounts to $2U_p$. The requirement to observe at least one FK oscillation in the dynamical regime is therefore $2U_p > \Lambda_{\text{FK}}$ or equivalently $\gamma > 0.6$. This result implies that quenching of the FK oscillations happens in the nonadiabatic regime, as demonstrated in Fig. 9(d).

Under this condition, we assess the sensitivity of the FK oscillation period in the cycle-average spectra to the e - h reduced mass. To this end, we compute the DFKE model for different reduced masses, with other parameters being fixed. Figures 10(a) and 10(b) compare the DFKE calculations with the adiabatic FK approximation, showing the influence of the reduced mass on FK oscillations. Figure 10(c) compares

the DFKE transparency width (black circles) as a function of reduced mass to Eq. (8) (black solid line) as well as the experimental value (magenta square). The discontinuity of the DFKE curve at the effective mass of 0.2 m_e is due to the ponderomotive potential impacting the oscillation width, which is also evident in Fig. 10(a). These results confirm that the standard electroabsorption analysis can also be applied in the dynamical FK regime, with the DFKE model [19].

We also note that the cycle-averaged (DC) part can be observed even with probe pulses that do not have subcycle resolution realized, i.e., with probe pulses of femtosecond duration.

VI. CONCLUSIONS AND OUTLOOK

We have presented the spectroscopic analysis of attosecond transient absorption measurements in fused silica. A dynamical FK model provides a simple parameterization of the nonequilibrium dielectric constant, while the *ab initio* calculation of the α -quartz response exhibits fine features due to multiple overlapping transitions that are absent in the experimental data because of finite temporal and spatial coherence and randomized orientation. Further, employing the DFKE model, we have clarified the origin of the characteristic *fishbone* time-energy absorption dependence and suggested its quantum limit. We have derived algebraic expressions for the DFKE as a $\chi^{(3)}$ process in a perturbative limit. By analyzing the time-dependent as well as cycle-averaged spectra, the band edges, electron-hole reduced mass, and the field strength are obtained in agreement with the literature values. Therefore, attosecond transient absorption spectroscopy is expected to provide direct experimental access to fast changes to the effective mass and the electron-hole binding energy during phase transitions and other ultrafast material distortions, such as exciton self-trapping in more complex materials. By analogy with the development of quasistatic electroabsorption, we expect finer features of the electronic structure, such as band anisotropy or electron-hole coherence, to become directly accessible in well-oriented crystals or quantum wells. For materials that are difficult to evaluate with *ab initio* methods, such as amorphous or strongly correlated solids, our analysis could provide useful model parameters for predicting their petahertz optical response, e.g., in optoelectronic applications.

The GUI application and the open-source MATLAB (MathWorks, Inc.) code for the DFKE calculation is available under GNU General Public License v3.0 [53].

ACKNOWLEDGMENTS

This paper was supported by the National Center of Competence in Research Molecular Ultrafast Science and Technology and funded by the Swiss National Science Foundation Project No. 200020_200416. This paper was supported by Japan Society for the Promotion of Science KAKENHI Grant No. JP20K14382. This paper has received funding from European Union's Horizon 2020 under Marie Skłodowska-Curie Action Grant No. 801459, FP-RESOMUS. This paper was supported by the European Research Council (No. ERC-2015-AdG694097), the Cluster of Excellence CUI:

Advanced Imaging of Matter of the Deutsche Forschungsgemeinschaft No. EXC 2056, Project ID No. 390715994, Grupos Consolidados UPV/EHU (No. IT1249-19), partially by the Federal Ministry of Education and Research Grant No. RouTe-13N14839, and the SFB925 “Light induced dynamics and control of correlated quantum systems,” by The Flatiron Institute, a division of the Simons Foundation.

APPENDIX A: ADDITIONAL EXPERIMENTAL DATA

We have also performed measurements in thicker 100-nm SiO₂ membranes [Fig. 3(b)] from a different supplier (G-Flat SiO₂, TEM windows). Low transmission affects the signal-to-noise ratio adversely; however, the transient absorption spectrogram shows the same features as the 40-nm foils discussed in the main text [Fig. 3(a)].

Measurement with a single attosecond pulse also confirms the main observation found with pulse trains, albeit with a lower signal-to-noise [Figs. 3(c) and 3(d)].

APPENDIX B: FIRST-PRINCIPLES ELECTRON DYNAMICS CALCULATIONS FOR TRANSIENT ABSORPTION SPECTROSCOPY OF α -QUARTZ

The transient absorption spectra of α -quartz are analyzed with the first-principles electron dynamics calculation based on TDDFT [54]. Here, we briefly describe the method used in this paper, while the details are described elsewhere [42].

To describe light-induced electron dynamics in solids, we employ the following time-dependent Kohn-Sham equations:

$$i\frac{\partial}{\partial t}u_{bk}(\mathbf{r}, t) = \left\{ \frac{1}{2}[\mathbf{p} + \mathbf{k} + \mathbf{A}(t)]^2 + \hat{v}_{\text{ion}} + v_H(\mathbf{r}, t) + v_{xc}(\mathbf{r}, t) \right\} u_{bk}(\mathbf{r}, t), \quad (\text{B1})$$

where $u_{bk}(\mathbf{r}, t)$ are time-dependent Bloch orbitals with the band index b and the Bloch wave vector \mathbf{k} . The Hamiltonian involves the time-dependent vector potential $\mathbf{A}(t)$, which is related to the external electric field as $\mathbf{E}(t) = -d\mathbf{A}(t)/dt$. To describe the electron-ion interaction \hat{v}_{ion} , we employ the norm-conserving pseudopotential method [55,56]. Here, $v_H(\mathbf{r}, t)$ denotes the time-dependent Hartree potential, and $v_{xc}(\mathbf{r}, t)$ denotes the exchange-correlation potential. In this paper, we employ the meta-generalized gradient approximation exchange-correlation potential [57] as $v_{xc}(\mathbf{r}, t)$ in the real-time TDDFT calculation [58].

For practical electron dynamics calculations in α -quartz, we employ a cuboid unit cell of dimensions $9.28 \times 16.05 \times 10.21$ a.u.³. The cuboid cell is discretized into $31 \times 54 \times 34$ grid points. The first Brillouin zone is discretized into $8 \times 4 \times 8$ k-points. All the *ab initio* simulations in this paper are performed with the SALMON code [59].

To evaluate the static absorption spectrum of α -quartz, we compute the electron dynamics under an impulsive distortion $\mathbf{E}(t) = E_0 \mathbf{e}_j \delta(t)$, where E_0 is the amplitude of the distortion, and \mathbf{e}_j is the unit-vector along j axis. As a result of the electron dynamics calculation, the electric current $\mathbf{J}(t)$ is obtained. In the weak field regime ($E_0 \rightarrow 0$), the current and

field are connected with the following relation:

$$J_i(\omega) = \sum_j \sigma_{ij}(\omega) E_j(\omega), \quad (\text{B2})$$

where $E_i(\omega)$ and $J_i(\omega)$ are i th component of the Fourier transform of $\mathbf{E}(t)$ and $\mathbf{J}(t)$, respectively. The optical conductivity $\sigma_{ij}(\omega)$ is related to the dielectric tensor as

$$\epsilon_{ij}(\omega) = \delta_{ij} + 4\pi i \frac{\sigma(\omega)}{\omega}. \quad (\text{B3})$$

We further evaluate the orientation averaged dielectric function as $\epsilon(\omega) = \frac{1}{3}[\epsilon_{xx}(\omega) + \epsilon_{yy}(\omega) + \epsilon_{zz}(\omega)]$ and calculate the optical absorption spectrum based on $\epsilon(\omega)$. The computed absorption spectrum of α -quartz is shown in Fig. 1(d) in the main text. To analyze the many-body effect, we computed the absorption spectrum of α -quartz with the IP approximation, where the time-dependence of $v_H(\mathbf{r}, t)$ and $v_{xc}(\mathbf{r}, t)$ are ignored, and these potentials are frozen at $t = 0$. The result of the IP approximation is also shown in Fig. 1(d) in the main text.

To evaluate the transient absorption spectra of α -quartz under the presence of the pump fields, we employ the *ab initio* numerical pump-probe scheme [60], with the two laser pulses: One is the pump pulse, while the other is the probe pulse. In this paper, we employ the following form for the vector potential of the pump pulse:

$$\mathbf{A}_{\text{pump}}(t) = -\frac{E_{\text{pump}}}{\Omega} \mathbf{e}_j \cos^2 \left[\frac{\pi t}{T_{\text{pump}}} \right] \sin[\Omega t] \quad (\text{B4})$$

in the domain, where $-T_{\text{pump}}/2 < t < T_{\text{pump}}/2$, and zero outside. Here, we set the pump field strength E_{pump} to 8.68×10^9 V/m, the mean photon energy $\hbar\Omega$ to 1.55 eV, and the pulse duration T_{pump} to 20 fs. Likewise, we employ the following form for the vector potential of the probe pulse:

$$\mathbf{A}_{\text{probe}}(t) = -\frac{E_{\text{probe}}}{\omega} \mathbf{e}_j \cos^4 \left[\frac{\pi}{T_{\text{probe}}} (t - T_{\text{delay}}) \right] \sin[\omega t] \quad (\text{B5})$$

in the domain, where $-T_{\text{probe}}/2 < t < T_{\text{probe}}/2$, and zero outside. Here, we set the probe field strength E_{probe} to 2.75×10^8 V/m, the mean photon energy $\hbar\omega$ to 30 eV, and the pulse duration T_{probe} to 1 fs. To compute the transient absorption spectra, we repeat the electron dynamics simulation with $\mathbf{A}_{\text{pump}}(t)$ and $\mathbf{A}_{\text{probe}}(t)$ by changing the time delay T_{delay} and evaluate the transient dielectric function for each delay according to the previous work [60]. The computed transient absorption spectra are shown in Fig. 2(d) in the main text.

APPENDIX C: ORIENTATION DEPENDENCE AND BAND DECOMPOSITION

To identify different contributions to the *ab initio* transient absorption, we present calculations performed along the α -quartz a axis [Fig. 4(a)] and c axis [Fig. 4(b)] separately. Most strikingly, we observe a modulation of the absorption with a periodicity of the infrared pump frequency Ω in the a -axis calculations. This reflects the broken inversion symmetry of α -quartz. A system with inversion symmetry would modulate at twice the infrared frequency. Further, we isolate the contribution of the transitions originating at the O 2s

level for the two corresponding crystal orientations, shown in Figs. 4(c) and 4(d). We find that the breaking of the inversion symmetry remains in the a -axis orientation; however, the O $2s$ contribution is overall different from the full calculation. Therefore, other transitions from the O $2p$ levels to high-lying states in the conduction band must be involved.

We compare the *ab initio* calculations with the DFKE model, using parabolic fits of the theoretical band structure in the latter. Parabolic fits of the *ab initio* band structure of α -quartz in the Γ -A direction yield >60 conduction and valence band pairs with a wide range of reduced masses, see Fig. 5(d), blue crosses. To simplify the analysis, we perform k -means clustering of the energy-mass data. With 22 band pairs [$k = 22$, Fig. 5(d), violet circles], the DFKE model [Fig. 5(b)] is in reasonable agreement with the *ab initio* calculation

[Fig. 5(a)]. Less accurate clustering [$k = 5$, Fig. 5(d), magenta squares], however, does not provide such agreement [Fig. 5(c)].

APPENDIX D: HIGHER-ORDER COMPONENTS OF THE DFKE

Figure 7 compares the AC parts of the DFKE in the nonperturbative ($I = 7$ TW/cm²) and perturbative regimes ($I = 0.07$ TW/cm²). The tilt of the spectral structure is higher for the 4Ω component by a factor of 2 compared with the 2Ω component. The spectral amplitudes of the in-phase and out-of-phase components (red and blue curves) oscillate with $2\hbar\Omega$ periodicity in all cases, due to the $\hbar\Omega$ spacing of the underlying Floquet-Bloch states.

APPENDIX E: PERTURBATIVE DERIVATION OF THE DFKE

Here, we show that the *fishbone* structure can be expressed in terms of third-order susceptibility. First, we briefly repeat the conclusive equations describing the DFKE [19]. The general expression for the real part of transient conductivity is derived in Ref. [19] and given by

$$Re\sigma_{2m}(\omega, t) = \frac{1}{4\pi\epsilon_0} \frac{e^2|p|^2}{\sqrt{2}\pi^2 m_e^2} \left(\frac{\mu}{\hbar^2}\right)^{3/2} \frac{1}{\omega + 2m\Omega} [C_{2m\Omega} \cos(2m\Omega t) + S_{2m\Omega} \sin(2m\Omega t)]. \quad (E1)$$

Here, e is the elementary charge, μ is the reduced electron-hole mass, $|p|^2$ is the matrix element for the valence-to-conduction band transition, m_e is electron mass, $\hbar\omega$ and $\hbar\Omega$ are probe and pump photon energies, $m = 0, \pm 1, \pm 2, \dots$, and

$$C_m(\omega) = \sum_l \pi [\sqrt{\epsilon_k^+} \xi_{l,2m}(k^+) - \sqrt{\epsilon_k^-} \xi_{l,-2m}(k^-)], \quad (E2)$$

$$k = \sqrt{2\mu\epsilon_k}, \quad (E3)$$

$$\epsilon_k^\pm = \pm(\omega + 2m\hbar\Omega) - (\epsilon_g + U_p + l\hbar\Omega). \quad (E4)$$

Coefficients $S_m(\omega)$ are obtained by principal value integration over resonant terms, which result from contour integration. The integrals can be calculated numerically via antithetic integration but are easier obtained via a Hilbert transform [13] that connects real and imaginary parts of conductivity via Kramers-Kronig relations.

In the following, while calculating $C_m(\omega)$ coefficients, we neglect the $\sqrt{\epsilon_k^-} \xi_{l,-2m}(k^-)$ terms that correspond to XUV emission:

$$C_m(\omega) = \pi \sum_l \sqrt{\Delta\epsilon + 2m\hbar\Omega - l\hbar\Omega} \xi_{l,2m}(\sqrt{2\mu} \sqrt{\Delta\epsilon + 2m\hbar\Omega - l\hbar\Omega}), \quad (E5)$$

where $\Delta\epsilon = \hbar\omega - \epsilon_g - U_p$. We see that the transition amplitude $C_m(\omega)$ is a product of the square-root JDOS and the overlap integrals $\xi_{l,2m}$:

$$\xi_{l,2m} = \int_{-1}^1 d(\cos\theta_{kA}) J_l(\theta_1, \theta_2) J_{l-2m}(\theta_1, \theta_2). \quad (E6)$$

Here, $J_l(\theta_1, \theta_2)$ are generalized Bessel functions $\theta_1 = \frac{e\vec{k}\vec{A}_0}{\mu c\Omega}$ and $\theta_2 = \frac{e^2 A_0^2}{8\mu c^2 \Omega} = \frac{1}{2}\gamma$.

The integral performs orientation averaging over the angles θ_{kA} between the quasimomentum \vec{k} and the vector potential \vec{A} . After orientation averaging, the overlap integrals can be expressed as functions of energy:

$$\xi_{l,2m}(\omega) = \xi_{l,2m} \left(\frac{eA_0}{\mu c\Omega} \sqrt{2\mu\epsilon_k}, \theta_2 \right). \quad (E7)$$

We use the approximation for the generalized Bessel functions, see Ref. [61], appendix J. This approximation is valid for a small second argument $\theta_2 = 0.5\gamma \ll 1$:

$$J_l(\theta_1, \theta_2) \approx J_l(\theta_1) + 0.5\theta_2[J_{l-2}(\theta_1) - J_{l+2}(\theta_1)]. \quad (E8)$$

TABLE II. Taylor expansion coefficients of Bessel products in Eq. (E11).

$C_{ l + l\mp 2 }$	$\frac{2}{ l + l\mp 2 +1} \text{sign}(l)^{ l } \text{sign}(l \mp 2)^{ l\mp 2 } \frac{1}{ l !} \frac{1}{ l\mp 2 !} \left(\frac{1}{2}\right)^{ l + l\mp 2 }$
$C_{ l + l\mp 2-2 }$	$0.5 \frac{2}{ l + l\mp 2-2 +1} \text{sign}(l)^{ l } \text{sign}(l \mp 2-2)^{ l\mp 2-2 } \frac{1}{ l !} \frac{1}{ l\mp 2-2 !} \left(\frac{1}{2}\right)^{ l + l\mp 2-2 }$
$C_{ l\mp 2 + l-2 }$	$0.5 \frac{2}{ l\mp 2 + l-2 +1} \text{sign}(l \mp 2)^{ l\mp 2 } \text{sign}(l-2)^{ l-2 } \frac{1}{ l\mp 2 !} \frac{1}{ l-2 !} \left(\frac{1}{2}\right)^{ l\mp 2 + l-2 }$
$C_{ l + l\mp 2,0+2 }$	$-0.5 \frac{2}{ l + l\mp 2+2 +1} \text{sign}(l)^{ l } \text{sign}(l \mp 2+2)^{ l\mp 2+2 } \frac{1}{ l !} \frac{1}{ l\mp 2+2 !} \left(\frac{1}{2}\right)^{ l + l\mp 2+2 }$
$C_{ l\mp 2,0 + l+2 }$	$-0.5 \frac{2}{ l\mp 2 + l+2 +1} \text{sign}(l \mp 2)^{ l\mp 2 } \text{sign}(l+2)^{ l+2 } \frac{1}{ l\mp 2 !} \frac{1}{ l+2 !} \left(\frac{1}{2}\right)^{ l\mp 2 + l+2 }$

Since 2Ω oscillations are dominant, we only consider $m = 0, \pm 1$. Further, neglecting the terms proportional to θ_2^2 , the products of the generalized Bessel function then take the form:

$$J_l(\theta_1, \theta_2) J_{l-2m}(\theta_1, \theta_2) = J_l(\theta_1) J_{l\mp 2}(\theta_1) + 0.5\theta_2 [J_l(\theta_1) J_{l\mp 2-2}(\theta_1) + J_{l\mp 2}(\theta_1) J_{l-2}(\theta_1) - J_l(\theta_1) J_{l\mp 2+2}(\theta_1) - J_{l\mp 2}(\theta_1) J_{l+2}(\theta_1)]. \quad (\text{E9})$$

Spatial integrals can now, in principle, be calculated with generalized hypergeometric functions [62]. To obtain simple expressions in the low-field regime, the Bessel functions can be further Taylor-expanded using the formula:

$$J_l(\theta_1) \approx \text{sign}(l)^l \frac{1}{|l|!} \left(\frac{\theta_1}{2}\right)^{|l|} - \text{sign}(l)^{|l|} \left(\frac{\theta_1}{2}\right)^{|l|} \frac{1}{(|l|+1)!} \left(\frac{\theta_1}{2}\right)^2. \quad (\text{E10})$$

After Taylor expansion, the orientation averaging can be calculated analytically noting that $2 \int_0^1 x^n dx = \frac{2}{n+1}$. With these approximations, we obtain

$$\xi_{l,\pm 2} = C_{|l|+|l\mp 2|} \theta_1^{|l|+|l\mp 2,0|} + \theta_2 \left[\begin{aligned} &C_{|l|+|l\mp 2-2|} \theta_1^{|l|+|l\mp 2,0-2|} + C_{|l\mp 2|+|l-2|} \theta_1^{|l\mp 2,0|+|l-2|} \\ &+ C_{|l|+|l\mp 2,0+2|} \theta_1^{|l|+|l\mp 2,0+2|} + C_{|l\mp 2,0|+|l+2|} \theta_1^{|l\mp 2,0|+|l+2|} \end{aligned} \right]. \quad (\text{E11})$$

The coefficients C are given in Table II.

Noting that θ_1 is linear with the field amplitude and θ_2 is quadratic, we regroup the terms proportional to the square of the electric field (Table III).

Therefore, in calculating $\xi_{l,2m}(\sqrt{2\mu}\sqrt{\Delta \in + 2m\hbar\Omega - l\hbar\Omega})$, for given indexes m, l :

$$\theta_1^2 = 2\mu \left(\frac{eA_0}{\mu c \hbar \Omega} \right)^2 (\Delta \in + 2m\hbar\Omega - l\hbar\Omega) = \frac{8\gamma}{\hbar\Omega} (\Delta \in + 2m\hbar\Omega - l\hbar\Omega). \quad (\text{E12})$$

We thus obtain the cosine-oscillating amplitudes:

$$C_{+1} = \frac{\gamma\pi}{2} \left(\frac{4}{3\hbar\Omega} \{(\Delta \in + 2\hbar\Omega)^{3/2} - 2(\Delta \in + \hbar\Omega)^{3/2} + (\Delta \in)^{3/2}\} + (\Delta \in)^{1/2} - (\Delta \in + 2\hbar\Omega)^{1/2} \right), \quad (\text{E13})$$

$$C_{-1} = \frac{\gamma\pi}{2} \left(\frac{4}{3\hbar\Omega} \{(\Delta \in - 2\hbar\Omega)^{3/2} - 2(\Delta \in - \hbar\Omega)^{3/2} + (\Delta \in)^{3/2}\} - (\Delta \in)^{1/2} + (\Delta \in - 2\hbar\Omega)^{1/2} \right), \quad (\text{E14})$$

$$C_0 = \gamma \frac{4\pi}{3\hbar\Omega} \{(\Delta \in - \hbar\Omega)^{3/2} + (\Delta \in + \hbar\Omega)^{3/2} - 2(\Delta \in)^{3/2}\} + 2\pi(\Delta \in)^{1/2}. \quad (\text{E15})$$

Here, we find terms that are proportional to the first or third power of the JDOS, e.g., $(\Delta \in)^{1/2}$ and $(\Delta \in)^{3/2}$. These terms correspond to single- or three-photon transitions. The three-photon transitions occur via intermediate resonances: single-photon (probe), two-photon (probe \pm pump), and three-photon (probe ± 2 pump), that correspond to the terms $(\Delta \in)^{3/2}$, $(\Delta \in \pm \hbar\Omega)^{3/2}$, and $(\Delta \in \pm 2\hbar\Omega)^{3/2}$. The expressions for DC amplitude C_0 reproduce the previously obtained expressions for the third-order

TABLE III. Taylor expansion coefficients of Bessel products in $\xi_{l,2m}(\omega)$ that are quadratic in the pump field amplitude.

	$l = -2$	$l = -1$	$l = 0$	$l = 1$	$l = 2$
$m = +1$			$\theta_1^2/12 - \theta_2$	$-\theta_1^2/6$	$\theta_1^2/12 - \theta_2$
$m = -1$	$\theta_1^2/12 - \theta_2$	$-\theta_1^2/6$	$\theta_1^2/12 + \theta_2$		
$m = 0$		$\theta_1^2/6$	$2 - \theta_1^2/4$	$\theta_1^2/6$	

nonlinearity at resonant interband transitions in the presence of nonresonant pump [50]. In this context, the terms are sometimes classified at electronic Raman ($\Delta \in -\hbar\Omega$)^{3/2}, two-photon absorption ($\Delta \in +\hbar\Omega$)^{3/2}, and Stark ($\Delta \in$)^{3/2}. We further note that the last DC term ($\Delta \in$)^{1/2} describes the ponderomotive shift of the band gap: $\Delta \in = \hbar\omega - \epsilon_g - U_p$ and involves only a single-photon (probe) transition.

The interpretation of the ($\Delta \in$)^{1/2}, ($\Delta \in \pm 2\hbar\Omega$)^{1/2} terms in the amplitudes of 2Ω -oscillating components $C_{\pm 1}$ is less transparent. Unlike the ($\Delta \in$)^{1/2} term in the C_0 coefficient described above, their contribution depends on the square of the electric field via the γ parameter:

$$C_{+1} \propto \gamma(\Delta \in)^{1/2} - \gamma(\Delta \in + 2\hbar\Omega)^{1/2} \propto E_0^2[(\Delta \in)^{1/2} - (\Delta \in + 2\hbar\Omega)^{1/2}], \quad (\text{E16})$$

and originates from the diamagnetic (ponderomotive) term of the Hamiltonian. However, the JDOS only appears in the first power (square root); thus, only a single-photon (probe) transition is involved. By analogy with the ($\Delta \in$)^{1/2} term in the C_0 coefficient, we can expect that these terms describe ponderomotive effects on the subcycle time scale. The maximum kinetic energy that the probe-created electron-hole pair can gain in the pump field is determined by the instant of its creation, set by the pump-probe delay. Therefore, the energy from the pump field can be transferred to the quasifree electron classically via intraband motion.

Noting that

$$C_{2m} \cos(2m\Omega t) + S_{2m} \sin(2m\Omega t) = \text{Im}\{(S_{2m} + iC_{2m})e^{i2m\Omega t}\}, \quad (\text{E17})$$

we obtain the third-order susceptibility of the dynamical FKE:

$$\chi^{(3)}(\omega, \pm\Omega, \pm\Omega) = \frac{1}{4\pi\epsilon_0} \frac{e^4 |p|^2 \sqrt{\mu/2}}{8\pi\hbar^3 m_0^2} \frac{1}{\omega^2 \Omega^2} (R_{\pm 1;0} + iI_{\pm 1;0}), \quad (\text{E18})$$

where

$$I_0 = \frac{8}{3\hbar\Omega} \{(\Delta \in - \hbar\Omega)^{3/2} + (\Delta \in + \hbar\Omega)^{3/2} - 2(\Delta \in)^{3/2}\}, \quad (\text{E19})$$

$$I_{+1} = \frac{4}{3\hbar\Omega} \{(\Delta \in + 2\hbar\Omega)^{3/2} - 2(\Delta \in + \hbar\Omega)^{3/2} + (\Delta \in)^{3/2}\} + (\Delta \in)^{1/2} - (\Delta \in + 2\hbar\Omega)^{\frac{1}{2}}, \quad (\text{E20})$$

$$I_{-1} = -I_{+1}(-\Omega). \quad (\text{E21})$$

Figure 8 compares the full DFKE calculation with the third-order approximation given by Eq. (E18), for $\gamma = 0.01$. We see a full reproduction of the fundamental *fishbone* shape and the relative approximation error of <4% [Figs. 8(c) and 8(d)].

-
- [1] H. Shen and F. H. Pollak, Generalized Franz-Keldysh theory of electromodulation, *Phys. Rev. B* **42**, 7097 (1990).
 - [2] H. Shen and M. Dutta, Franz-Keldysh oscillations in modulation spectroscopy, *J. Appl. Phys.* **78**, 2151 (1995).
 - [3] W. Franz, Einfluß eines elektrischen Feldes auf eine optische Absorptionskante, *Z. Naturforsch. A* **13**, 484 (1958).
 - [4] L. V. Keldysh, The effect of a strong electric field on the optical properties of insulating crystals, *J. Exptl. Theor. Phys.* **34**, 1138 (1958).
 - [5] J. Hader, N. Linder, and G. H. Döhler, $\mathbf{k} \cdot \mathbf{p}$ theory of the Franz-Keldysh effect, *Phys. Rev. B* **55**, 6960 (1997).
 - [6] F. Duque-Gomez and J. E. Sipe, The Franz-Keldysh effect revisited: Electroabsorption including interband coupling and excitonic effects, *J. Phys. Chem. Solids* **76**, 138 (2015).
 - [7] A. Jaeger and G. Weiser, Excitonic electroabsorption spectra and Franz-Keldysh effect of studied by small modulation of static fields, *Phys. Rev. B* **58**, 10674 (1998).
 - [8] P. Kiesel, T. Kippenberg, E. Greger, M. Moser, U. Hilburger, J. Krauss, G. Schmiedel, and G. H. Döhler, Valence band structure of ordered GaInP determined by polarization-dependent electroabsorption measurements, *Physica E* **2**, 599 (1998).
 - [9] R. N. Bhattacharya, H. Shen, P. Parayanthal, F. H. Pollak, T. Coutts, and H. Aharoni, Electroreflectance and photorefectance study of the space-charge region in semiconductors: (In-Sn-O)/InP as a model system, *Phys. Rev. B* **37**, 4044 (1988).
 - [10] A. Jaeger, G. Weiser, P. Wiedemann, I. Gyuro, and E. Zielinski, The sizes of coherent band states in semiconductors, derived from the Franz-Keldysh effect, *J. Phys.: Condens. Matter* **8**, 6779 (1996).
 - [11] H. J. Kolbe, C. Agert, W. Stolz, and G. Weiser, Coherence in real space: The transition range from bulk to confined states studied by the Franz-Keldysh effect, *Physica E* **6**, 173 (2000).
 - [12] G. C. Cho, H. J. Bakker, T. Dekorsy, and H. Kurz, Time-resolved observation of coherent phonons by the Franz-Keldysh effect, *Phys. Rev. B* **53**, 6904 (1996).
 - [13] Y. Yacoby, High-frequency Franz-Keldysh effect, *Phys. Rev.* **169**, 610 (1967).
 - [14] K. Johnsen and A.-P. Jauho, Nonequilibrium absorption in semiconductors and the dynamical Franz-Keldysh effect, *Phys. Scr.* **1997**, 177 (1997).
 - [15] D. S. Citrin and S. Hughes, Circularly polarized dynamic Franz-Keldysh effect, *Phys. Rev. B* **60**, 13272 (1999).
 - [16] K. Shinokita, H. Hirori, M. Nagai, N. Satoh, Y. Kadoya, and K. Tanaka, Dynamical Franz-Keldysh effect in GaAs/AlGaAs multiple quantum wells induced by single-cycle terahertz pulses, *Appl. Phys. Lett.* **97**, 211902 (2010).
 - [17] F. Novelli, D. Fausti, F. Giusti, F. Parmigiani, and M. Hoffmann, Mixed regime of light-matter interaction revealed by phase sensitive measurements of the dynamical Franz-Keldysh effect, *Sci. Rep.* **3**, 1227 (2013).

- [18] C. Schmidt, J. Bühler, A. C. Heinrich, J. Allerbeck, R. Podzinski, D. Berghoff, T. Meier, W. G. Schmidt, C. Reichl, W. Wegscheider *et al.*, Signatures of transient Wannier-Stark localization in bulk gallium arsenide, *Nat. Commun.* **9**, 2890 (2018).
- [19] T. Otake, Y. Shinohara, S. A. Sato, and K. Yabana, Femtosecond time-resolved dynamical Franz-Keldysh effect, *Phys. Rev. B* **93**, 045124 (2016).
- [20] M. Lucchini, S. A. Sato, A. Ludwig, J. Herrmann, M. Volkov, L. Kasmi, Y. Shinohara, K. Yabana, L. Gallmann, and U. Keller, Attosecond dynamical Franz-Keldysh effect in polycrystalline diamond, *Science* **353**, 916 (2016).
- [21] F. Schlaepfer, M. Lucchini, S. A. Sato, M. Volkov, L. Kasmi, N. Hartmann, A. Rubio, L. Gallmann, and U. Keller, Attosecond optical-field-enhanced carrier injection into the GaAs conduction band, *Nat. Phys.* **14**, 560 (2018).
- [22] M. Volkov, S. A. Sato, F. Schlaepfer, L. Kasmi, N. Hartmann, M. Lucchini, L. Gallmann, A. Rubio, and U. Keller, Attosecond screening dynamics mediated by electron localization in transition metals, *Nat. Phys.* **15**, 1145 (2019).
- [23] A. Niedermayr, M. Volkov, S. A. Sato, N. Hartmann, Z. Schumacher, S. Neb, A. Rubio, L. Gallmann, and U. Keller, Few-Femtosecond Dynamics of Free-Free Opacity in Optically Heated Metals, *Phys. Rev. X* **12**, 021045 (2022).
- [24] T. Otake, K. Yabana, and J.-I. Iwata, First-principles calculation of the electron dynamics in crystalline SiO₂, *J. Phys.: Condens. Matter* **21**, 064224 (2009).
- [25] G. Wachter, C. Lemell, J. Burgdörfer, S. A. Sato, X.-M. Tong, and K. Yabana, *Ab Initio* Simulation of Electrical Currents Induced by Ultrafast Laser Excitation of Dielectric Materials, *Phys. Rev. Lett.* **113**, 087401 (2014).
- [26] S. A. Sato and K. Yabana, Efficient basis expansion for describing linear and nonlinear electron dynamics in crystalline solids, *Phys. Rev. B* **89**, 224305 (2014).
- [27] N. Tancogne-Dejean, M. A. Sentef, and A. Rubio, Ultrafast transient absorption spectroscopy of the charge-transfer insulator NiO: Beyond the dynamical Franz-Keldysh effect, *Phys. Rev. B* **102**, 115106 (2020).
- [28] M. Lucchini, S. A. Sato, G. D. Lucarelli, B. Moio, G. Inzani, R. Borrego-Varillas, F. Frassetto, L. Poletto, H. Hübener, U. De Giovannini *et al.*, Unravelling the intertwined atomic and bulk nature of localised excitons by attosecond spectroscopy, *Nat. Commun.* **12**, 1021 (2021).
- [29] S. Sederberg, D. Zimin, S. Keiber, F. Siegrist, M. S. Wismer, V. S. Yakovlev, I. Floss, C. Lemell, J. Burgdörfer, M. Schultze *et al.*, Attosecond optoelectronic field measurement in solids, *Nat. Commun.* **11**, 430 (2020).
- [30] M. Garg, M. Zhan, T. T. Luu, H. Lakhota, T. Klostermann, A. Guggenmos, and E. Goulielmakis, Multi-petahertz electronic metrology, *Nature (London)* **538**, 359 (2016).
- [31] M. Schultze, E. M. Bothschafter, A. Sommer, S. Holzner, W. Schweinberger, M. Fiess, M. Hofstetter, R. Kienberger, V. Apalkov, V. S. Yakovlev *et al.*, Controlling dielectrics with the electric field of light, *Nature (London)* **493**, 75 (2013).
- [32] A. Moulet, J. B. Bertrand, T. Klostermann, A. Guggenmos, N. Karpowicz, and E. Goulielmakis, Soft x-ray excitonics, *Science* **357**, 1134 (2017).
- [33] T. T. Luu, M. Garg, S. Y. Kruchinin, A. Moulet, M. T. Hassan, and E. Goulielmakis, Extreme ultraviolet high-harmonic spectroscopy of solids, *Nature (London)* **521**, 498 (2015).
- [34] T. T. Luu and H. J. Wörner, Measurement of the berry curvature of solids using high-harmonic spectroscopy, *Nat. Commun.* **9**, 916 (2018).
- [35] P. Jürgens, B. Liewehr, B. Kruse, C. Peltz, D. Engel, A. Husakou, T. Witting, M. Ivanov, M. J. J. Vrakking, T. Fennel *et al.*, Origin of strong-field-induced low-order harmonic generation in amorphous quartz, *Nat. Phys.* **16**, 1035 (2020).
- [36] A. Sommer, E. M. Bothschafter, S. A. Sato, C. Jakubeit, T. Latka, O. Razskazovskaya, H. Fattahi, M. Jobst, W. Schweinberger, V. Shirvanyan *et al.*, Attosecond nonlinear polarization and light-matter energy transfer in solids, *Nature (London)* **534**, 86 (2016).
- [37] R. Locher, M. Lucchini, J. Herrmann, M. Sabbar, M. Weger, A. Ludwig, L. Castiglioni, M. Greif, M. Hengsberger, L. Gallmann *et al.*, Versatile attosecond beamline in a two-foci configuration for simultaneous time-resolved measurements, *Rev. Sci. Instrum.* **85**, 013113 (2014).
- [38] S. S. Nekrashevich and V. A. Gritsenko, Electronic structure of silicon dioxide (a review), *Phys. Solid State* **56**, 207 (2014).
- [39] D. J. Chadi, R. B. Laughlin, and J. D. Joannopoulos, Electronic structures of crystalline and amorphous SiO₂, in *The Physics of SiO₂ and Its Interfaces*, edited by S. T. Pantelides (Pergamon Press, New York, 1978), pp. 55–59.
- [40] H. G. Muller, Reconstruction of attosecond harmonic beating by interference of two-photon transitions, *Appl. Phys. B* **74**, s17 (2002).
- [41] M. Lucchini, S. A. Sato, F. Schlaepfer, K. Yabana, L. Gallmann, A. Rubio, and U. Keller, Attosecond timing of the dynamical Franz-Keldysh effect, *J. Phys. Photon.* **2**, 025001 (2020).
- [42] S. A. Sato, First-principles calculations for attosecond electron dynamics in solids, *Comput. Mater. Sci.* **194**, 110274 (2021).
- [43] S. A. Sato, H. Hübener, U. De Giovannini, and A. Rubio, *Ab initio* simulation of attosecond transient absorption spectroscopy in two-dimensional materials, *Appl. Sci.* **8**, 1777 (2018).
- [44] K. Uchida, T. Otake, T. Mochizuki, C. Kim, M. Yoshita, H. Akiyama, L. N. Pfeiffer, K. W. West, K. Tanaka, and H. Hirori, Subcycle Optical Response Caused by a Terahertz Dressed State with Phase-Locked Wave Functions, *Phys. Rev. Lett.* **117**, 277402 (2016).
- [45] M. Du, C. Liu, Y. Zheng, Z. Zeng, and R. Li, Attosecond transient-absorption spectroscopy in one-dimensional periodic crystals, *Phys. Rev. A* **100**, 043840 (2019).
- [46] F. Dong and J. Liu, Fishbone resonance structure in the attosecond transient absorption spectrum of graphene, *Phys. Rev. A* **106**, 063107 (2022).
- [47] G. Cistaro, L. Plaja, F. Martín, and A. Picón, Attosecond x-ray transient absorption spectroscopy in graphene, *Phys. Rev. Res.* **3**, 013144 (2021).
- [48] S. Y. Kruchinin, F. Krausz, and V. S. Yakovlev, Colloquium: Strong-field phenomena in periodic systems, *Rev. Mod. Phys.* **90**, 021002 (2018).
- [49] H. D. Jones and H. R. Reiss, Intense-field effects in solids, *Phys. Rev. B* **16**, 2466 (1977).
- [50] C. Aversa, J. E. Sipe, M. Sheik-Bahae, and E. W. Van Stryland, Third-order optical nonlinearities in semiconductors: The two-band model, *Phys. Rev. B* **50**, 18073 (1994).
- [51] K. Ekvall, P. van der Meulen, C. Dhollande, L. E. Berg, S. Pommeret, R. Naskrecki, and J. C. Mialocq, Cross phase

- modulation artifact in liquid phase transient absorption spectroscopy, *J. Appl. Phys.* **87**, 2340 (2000).
- [52] D. C. Hutchings, M. Sheik-Bahae, D. J. Hagan, and E. W. Van Stryland, Kramers-Krönig relations in nonlinear optics, *Opt. Quant. Electron.* **24**, 1 (1992).
- [53] <https://github.com/mikhailVvolkov/DFKE>.
- [54] E. Runge and E. K. U. Gross, Density-Functional Theory for Time-Dependent Systems, *Phys. Rev. Lett.* **52**, 997 (1984).
- [55] L. Kleinman and D. M. Bylander, Efficacious Form for Model Pseudopotentials, *Phys. Rev. Lett.* **48**, 1425 (1982).
- [56] N. Troullier and J. L. Martins, Efficient pseudopotentials for plane-wave calculations, *Phys. Rev. B* **43**, 1993 (1991).
- [57] F. Tran and P. Blaha, Accurate Band Gaps of Semiconductors and Insulators with a Semilocal Exchange-Correlation Potential, *Phys. Rev. Lett.* **102**, 226401 (2009).
- [58] S. A. Sato, Y. Taniguchi, Y. Shinohara, and K. Yabana, Nonlinear electronic excitations in crystalline solids using meta-generalized gradient approximation and hybrid functional in time-dependent density functional theory, *J. Chem. Phys.* **143**, 224116 (2015).
- [59] M. Noda, S. A. Sato, Y. Hirokawa, M. Uemoto, T. Takeuchi, S. Yamada, A. Yamada, Y. Shinohara, M. Yamaguchi, K. Iida *et al.*, SALMON: Scalable *ab-initio* light-matter simulator for optics and nanoscience, *Comput. Phys. Commun.* **235**, 356 (2019).
- [60] S. A. Sato, K. Yabana, Y. Shinohara, T. Otobe, and G. F. Bertsch, Numerical pump-probe experiments of laser-excited silicon in nonequilibrium phase, *Phys. Rev. B* **89**, 064304 (2014).
- [61] V. P. Krainov, H. R. Reiss, and B. M. Smirnov, *Radiative Processes in Atomic Physics* (John Wiley & Sons, Hoboken, 2005).
- [62] L. J. Landau and N. J. Luswili, Asymptotic expansion of a Bessel function integral using hypergeometric functions, *J. Comput. Appl. Math.* **132**, 387 (2001).